Impact of mesoscale eddy transfer heat uptake in an eddy-parameterizing ocean model

Article

Published Version

www.reading.ac.uk/centaur

CentAUR

Central Archive at the University of Reading

Reading's research outputs online

Impact of Mesoscale Eddy Transfer on Heat Uptake in an Eddy-Parameterizing Ocean Model

OLEG A. SAENKO AND DUO YANG

Canadian Centre for Climate Modelling and Analysis, Victoria, British Columbia, Canada

JONATHAN M. GREGORY

National Centre for Atmospheric Science, University of Reading, Reading, and Met Office Hadley Centre, Exeter, United Kingdom

ABSTRACT

Using a set of experiments with an eddy-parameterizing ocean model, it is found that the strength of the Atlantic meridional overturning circulation (AMOC) intensifies with the decrease of the density-dependent mesoscale eddy transfer. However, the intensification is weaker than that suggested by simple scaling relationships previously applied. Perturbing the model control sea surface temperature (SST) to mimic its change in response to doubling of CO_2, it is shown that the associated ocean heat uptake (OHU) increases and penetrates deeper with the decrease of the mesoscale eddy transfer. It is shown that the OHU correlates with the AMOC strength, and both these quantities are affected by the mesoscale eddy transfer. Passive tracer experiments in the ocean model provide a possible explanation for the finding in coupled-model climate simulations that the ocean heat uptake efficiency (OHUE) increases with the AMOC strength and decreases with the eddy energy generated from the mean state. It is also found that the OHU in the SST-perturbation experiments scales with the net downward advection of heat. The contribution of the AMOC to the downward heat flux is illustrated using a streamfunction in depth–temperature space.

1. Introduction

By removing heat from surface to subsurface layers, ocean dynamics play a key role in mitigating climate change in response to enhanced radiative forcing. Indeed, a substantial contribution to the observed ocean heat uptake (OHU) comes from the warming of subsurface layers (Levitus et al. 2012). The processes that transport heat vertically in the ocean include small-scale turbulence, convection, mesoscale and submesoscale eddy effects, and large-scale circulation [e.g., Ekman pumping and meridional overturning circulation (MOC)]. Some of these are only partly resolved in coupled atmosphere–ocean general circulation models (AOGCMs) employed for long-term climate simulations. Some are not resolved at all; instead, they are parameterized. The formulations and/or parameters used to represent ocean unresolved or partly resolved processes often differ between the models, contributing to the differences in the simulated OHU (Exarchou et al. 2015). Even such a global-scale feature as the Atlantic MOC (AMOC) shows a considerable range across AOGCMs in terms of its strength and depth. This contributes to the spread in the ocean heat uptake efficiency (OHUE; i.e., OHU per unit increase in surface warming) in climate change simulations (e.g., Kostov et al. 2014; Winton et al. 2014; J. M. Gregory et al. 2017, unpublished manuscript). The spread in the OHUE across AOGCMs is quite large, being a factor of 2 in the AOGCMs that participated in phase 3 of the Coupled Model Intercomparison Project (CMIP3) and phase 5 of the Coupled Model Intercomparison Project (CMIP5; Kuhlbrodt and Gregory 2012). How the AMOC is related to OHUE and why there is a correlation between the AMOC strength and OHUE in climate simulations based on AOGCMs (e.g., Kostov et al. 2014; Winton et al. 2014; J. M. Gregory et al. 2017, unpublished manuscript) has not as yet been comprehensively explained. One of the purposes here is to provide some insight on this important subject.

ⱂ Denotes content that is immediately available upon publication as open access.

Corresponding author: Oleg A. Saenko, oleg.saenko@canada.ca

Uncertainties in the formulations and/or parameters used to represent unresolved ocean processes can contribute to the uncertainties in the simulated OHU/OHUE not only directly, through affecting the associated heat fluxes, but also indirectly. The latter can arise because of the influence of parameterized processes on the large-scale ocean circulation, with one familiar example being the impact of vertical diffusivity on the MOC (e.g., Wunsch and Ferrari 2004). Another example is the representation of mesoscale eddy transfer, which is our focus here. Studies where ocean mesoscale eddy effects have been resolved to some extent (Wolfe et al. 2008; Morrison et al. 2013; Kuhlbrodt et al. 2015; Griffies et al. 2015) confirmed an earlier result of Gregory (2000) that eddies play a major part in the vertical transport of heat in the ocean. The indirect effects associated with representation of ocean mesoscale eddies on the simulated OHU have been studied somewhat less extensively. Here, we aim to investigate further the apparent link between the mesoscale eddy transfer coefficient in the Gent and McWilliams (1990) scheme (see section 2), which is often employed for representing eddy-induced ocean transport, and the AMOC and OHU. This is motivated by several studies that showed relationships 1) between the mesoscale eddy transfer coefficient and OHUE/OHU (Kuhlbrodt and Gregory 2012; Marshall and Zanna 2014), 2) between OHUE and AMOC (e.g., Kostov et al. 2014; Winton et al. 2014; J. M. Gregory et al. 2017, unpublished manuscript), and 3) between the AMOC and mesoscale eddy transfer (e.g., Gnanadesikan 1999; Marshall et al. 2017). Combined, these previous studies suggest that some of the apparent correlation between the OHUE and AMOC strength could arise because of the influence of the ocean mesoscale eddy transfer on both these quantities. Here, we aim to provide a further support for this suggestion. However, to present our main finding in a systematic way, we feel that it is essential to demonstrate that the main pieces of our argument, if considered separately, are consistent with these previous results. We try to ensure this throughout the paper.

To analyze a range of numerical experiments, some of which require running a model to near-steady state, we adopt an ocean-only modeling approach. This is certainly a simplification compared to the use of AOGCMs. Nevertheless, employing ocean-only models to study OHU processes can be quite insightful (e.g., Xie and Vallis 2012; Marshall et al. 2015). To simulate OHU, we force our model with sea surface temperature (SST) anomalies that are meant to mimic the impact of CO_2 increase in the atmosphere. Section 2 provides more details on the experimental design and employed model, including on the formulation for the mesoscale eddy transfer.

Unlike in some previous studies where a horizontally uniform mesoscale eddy transfer coefficient was used in relation with the AMOC (e.g., Gnanadesikan 1999; Marshall et al. 2017), we employ a density-dependent formulation. This allows for a feedback between the simulated density field and the mesoscale eddy transfer. Section 3 begins with a discussion of different components of the global ocean MOC and how they are influenced by the mesoscale eddy transfer in a set of 1000-yr control simulations. In particular, it is found that with the decrease of the eddy transfer coefficient, the strength of the AMOC increases. This is in general agreement with Gnanadesikan (1999) and Marshall et al. (2017), whose scaling relations are employed to interpret our results. This is followed by a discussion of sensitivity experiments where the simulated control ocean states are perturbed by imposing SST anomalies. It is shown that the associated OHU correlates with the AMOC strength and, hence, anticorrelates with the mesoscale eddy transfer. Simulations with a surface-forced passive tracer are used to argue that OHUE is linked to the ocean mesoscale eddy transfer and to the eddy energy generated from the mean state. In section 4, a special consideration is given to the ocean overturning in depth–temperature space, which represents the advective vertical heat transport (e.g., Nycander et al. 2007; Zika et al. 2013, 2015), and to its connection to the AMOC. Conclusions are summarized in section 5.

2. Model and experimental design

The employed model is a low-resolution configuration of the Nucleus for European Modelling of the Ocean, version 3.4 (NEMO; Madec et al. 2012). The model uses a free-surface formulation and is configured on the global tripolar ORCA1 grid with 46 z-coordinate vertical levels. The horizontal resolution is 1°, varying with the cosine of latitude, with a refinement of the meridional grid spacing to ⅓° near the equator. Momentum and tracers are mixed vertically using a TKE scheme based on the model of Gaspar et al. (1990). Base values of vertical diffusivity and viscosity are 1.5×10^{-5} and $1.5 \times 10^{-4} \, m^2 \, s^{-1}$, respectively. Tidal mixing is parameterized following Simmons et al. (2004). Lateral viscosity is parameterized by a horizontal Laplacian operator with eddy viscosity coefficient of $10^4 \, m^2 \, s^{-1}$ in the tropics, decreasing with latitude as the grid spacing decreases. Lateral mixing of tracers (Redi 1982) is parameterized by an isoneutral Laplacian operator with eddy diffusivity coefficient of $K_{Redi} = 10^3 \, m^2 \, s^{-1}$ near the equator, which decreases poleward with the cosine of latitude. In all model experiments K_{Redi} is kept unchanged. Instead, the focus is on

the mesoscale eddy transfer coefficient in the Gent and McWilliams (1990) scheme K_{GM}. In the spirit of Gnanadesikan et al. (2015), we assume that K_{Redi} is not the same as K_{GM}. The Gent and McWilliams (1990) scheme is meant to represent the process of extraction of potential energy by baroclinic instability. Unlike K_{Redi}, K_{GM} would affect the transport of heat even if ocean density were a function of temperature only.

We use K_{GM}, which varies in space (only horizontally) and time. It is given by (e.g., Visbeck et al. 1997; Bryan et al. 1999)

$$K_{GM} = L^2 T^{-1}, \qquad (1)$$

where L is a mixing length scale and

$$T^{-1} = \frac{1}{H} \int_{-H}^{0} \frac{|\nabla \overline{b}|}{\sqrt{\overline{b}_z}} dz \qquad (2)$$

is the inverse time scale (local growth rate) associated with baroclinic eddies, with $\overline{b}$ being the model-resolved buoyancy field and ∇ representing the horizontal gradient operator. It is not uncommon to assume (e.g., Cessi 2008) that

$$L = L_r = \frac{1}{\pi |f|} \int_{-H}^{0} N \, dz, \qquad (3)$$

where L_r is the first baroclinic Rossby radius of deformation and $N = \sqrt{\overline{b}_z}$ is the buoyancy frequency. Combining (1)–(3) gives

$$K_{GM} = \frac{1}{(\pi f)^2} \frac{1}{H} \int_{-H}^{0} \frac{|\nabla \overline{b}|}{\sqrt{\overline{b}_z}} dz \left(\int_{-H}^{0} \sqrt{\overline{b}_z} \, dz \right)^2. \quad (4)$$

Here, instead, we assume that the mixing length is given by the eddy scale L_e. Recent observational estimates suggest that typically $L_e > L_r$, which could be due to the inverse energy cascade (Chelton et al. 2011). In particular, the Rossby radius and eddy scale are comparable in the tropical regions, having values on the order of 200 km (e.g., Chelton et al. 2011; their Fig. 12). However, toward the midlatitudes, the Rossby radius decreases more rapidly than does the eddy scale (Fig. 1). Based on this observational evidence, and to retain a dependence of K_{GM} on L_r, we assume that

$$L_e \propto L_r^{\alpha}, \qquad (5)$$

where $0 < \alpha < 1$. This gives

$$K_{GM} = \frac{c}{(\pi f)^{2\alpha}} \frac{1}{H} \int_{-H}^{0} \frac{|\nabla \overline{b}|}{\sqrt{\overline{b}_z}} dz \left(\int_{-H}^{0} \sqrt{\overline{b}_z} \, dz \right)^{2\alpha}, \quad (6)$$
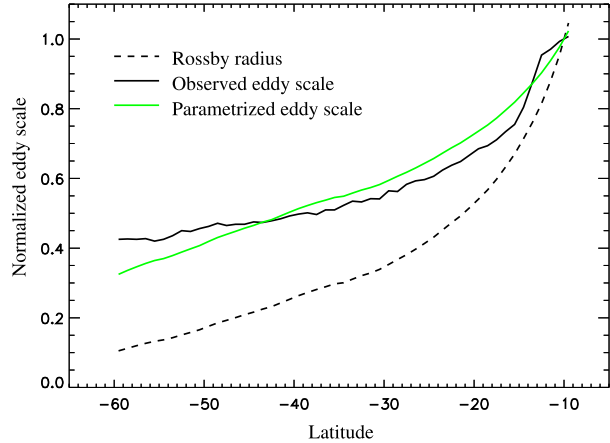

FIG. 1. Meridional profiles of observational estimate of eddy scale based on altimetry data (solid) and L_r (dashed), both from Chelton et al. (2011, their Fig. 12). The green curve represents the profile of $L_e \propto L_r^{1/2}$, which is used to parameterize the eddy scale in the model when computing the eddy transfer coefficient K_{GM} (see text for details). The scales correspond to the Southern Hemisphere and are normalized by their values at 10°S.

where c is a dimensional constant. In our model, same as in Stanley and Saenko (2014), we set $\alpha = 0.5$. This gives a reasonably good fit of L_e to the observed eddy scale (Fig. 1). In such case c in (6) has the units of length. We further assume that $c = l\gamma$, where l is some prescribed length scale (a "typical" eddy scale, set to 50 km) and γ is a nondimensional tuning parameter (or scale factor). The latter is varied in the model experiments to be discussed, to change K_{GM}, with one of the expected effects being a change in the strength of the MOC (Marshall et al. 2017).

The spatial structure of K_{GM} is displayed in Fig. 2 (left). As expected, the largest values are found in the regions of western boundary currents and in the Southern Ocean. In the model experiments discussed below, K_{GM} is constrained not to drop below $100 \, \mathrm{m^2 \, s^{-1}}$. In the tropics, an additional constraint is applied that ensures that the values of K_{GM} there are only slightly higher than the minimum value of $100 \, \mathrm{m^2 \, s^{-1}}$. One reason for this is that in the tropics the transient ocean variability is thought to be dominated by the tropical instability waves, rather than by baroclinic eddies. The model grid refinement in the tropics is aimed, in part, at capturing some portion of this variability.

The model restores SST T_s and sea surface salinity S_s to their daily climatologies T^* and S^* with restoring time scales of about 10 and 45 days, respectively. The net fluxes of heat and salinity at the surface are the sum of the corresponding restoring terms and imposed background fluxes of heat and water. The background fluxes of heat and water as well as the imposed momentum flux
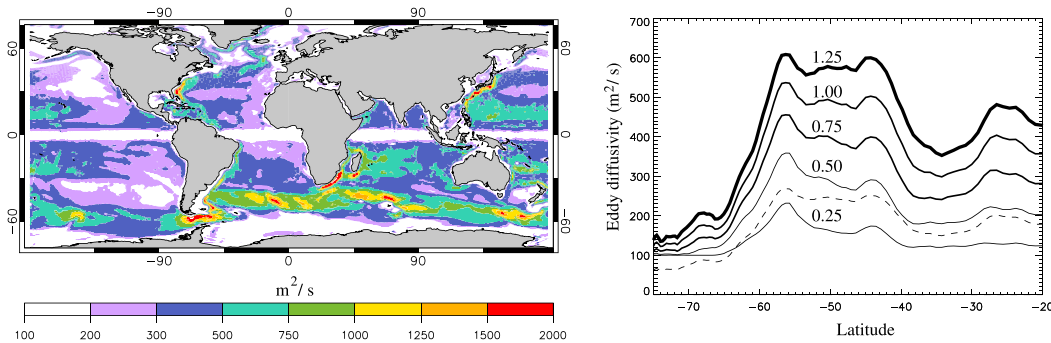
FIG. 2. (left) The spatial structure of time-mean K_{GM} computed using (6) in the model control run where the tuning parameter γ is set to 1.25. (right) Meridional structure of the zonally averaged K_{GM} in the Southern Ocean in the five control runs with γ decreasing from 1.25 (thickest curve) to 0.25 (thinnest curve). The dashed curve corresponds to K_{GM} with $\gamma = 1.00$, scaled by a factor of 0.5; this is to illustrate the difference from K_{GM} with $\gamma = 0.5$.

are kept unchanged in the model experiments discussed here. All surface forcing fields are derived from a historical simulation based on the Second Generation Canadian Earth System Model (CanESM2; e.g., Yang and Saenko 2012) and averaged from 1979 to 2005 to form daily climatology. Five control experiments (Controls) were run for 1050 years, with the only difference between them being the value of the scale factor γ in the representation of K_{GM}, as described above. This was motivated by our desire to change K_{GM}, so that the AMOC strength would differ between our control runs, as expected based on the scaling theory of Gnanadesikan (1999). However, since K_{GM} is not horizontally uniform in our model [unlike in Gnanadesikan (1999) and Marshall et al. (2017)], but depends on the simulated density field [(6)], we use the tuning parameter γ to change K_{GM}. Specifically, we set γ to 1.25, 1.00, 0.75, 0.50, and 0.25. The corresponding meridional profiles of K_{GM} in the Southern Ocean are presented in Fig. 2 (right). The range of the simulated K_{GM} values is well within their ranges in the CMIP3 and CMIP5 models (Kuhlbrodt and Gregory 2012; Huber and Zanna 2017).

It should be noted that, aside from the energy removed by baroclinic instability from the mean ocean state E_{eddy}, there are very few other constrains on K_{GM}. For the eddies parameterized with the Gent and McWilliams (1990) scheme, the global rate with which they extract potential energy from the mean ocean state can be estimated as follows (e.g., Gent et al. 1995; Wunsch and Ferrari 2004):

$$E_{eddy} = \rho_0 \iiint K_{GM} \left(\frac{|\nabla \overline{b}|}{N} \right)^2 dV, \qquad (7)$$

where ρ_0 is the ocean reference density. Using hydrographic climatology for the density field, an estimate for E_{eddy} based on (7) could vary from 0.2 to 1.3 TW,

depending on the assumptions about K_{GM} (Wunsch and Ferrari 2004). In our control runs, E_{eddy} varies from 0.55 TW in the case of the smallest K_{GM} to 0.98 TW in the case of the largest K_{GM} (regions with very weak stratification, where $N^2 < 10^{-8}\,\mathrm{s}^{-2}$ and that occupy less than 5% of the ocean volume in our simulations, were excluded from this calculation). Therefore, at least on these grounds, using any of the adopted values for the tuning parameter γ can be justified.

To investigate the relationship between K_{GM} and OHU, for each of the five control experiments we run two sets of 50-yr-long sensitivity experiments, starting at year 1001. In these experiments, the restoring SST T^* is abruptly changed by ΔT^*, leading to the surface heat flux anomaly of

$$\Delta Q^h = \lambda (\Delta T^* - \Delta T_s), \qquad (8)$$

where λ is the restoring parameter. This ocean perturbation procedure is similar to, but not quite the same as in, one of the sensitivity experiments discussed by Xie and Vallis (2012; who used an idealized basin ocean model). In the first set of sensitivity experiments (hereafter Simple), the restoring SSTs are modified to increase uniformly by 2 K between 60°S and 70°N (i.e., roughly outside of the ice covered regions). In the second set of sensitivity experiments (hereafter Complex), the restoring SSTs correspond to their changes simulated by CanESM2 in the 1% yr^{-1} CO_2-increase experiment, averaged over 20 years at the time of CO_2 doubling (years 61–80; Fig. 3). In all model experiments, the surface salinity flux is not changed explicitly (i.e., $\Delta S^* = 0$), although it can change implicitly because of changes in S_s.

One of the purposes of running two sets of sensitivity experiments was to find out if using a highly idealized ΔT^* in Simple could capture the large-scale structure of the OHU corresponding to a more realistic ΔT^* in
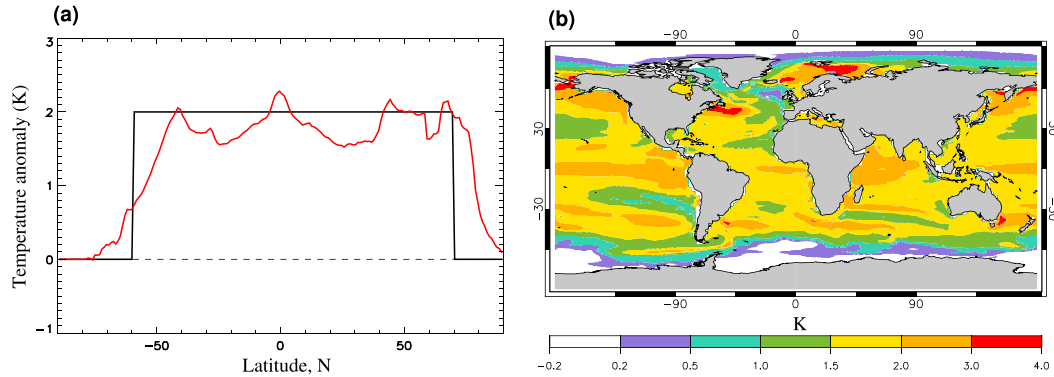
FIG. 3. (a) Meridional structure of annual-mean SST anomalies ΔT^* applied in Simple (black) and Complex (red) sets of the model sensitivity experiments (see text for details). (b) Spatial structure of the mean ΔT^* in the Complex set of experiments. It corresponds to a 20-yr-mean SST anomaly simulated by CanESM2 in the 1% yr^{-1} CO_2-increase experiment, averaged at CO_2 doubling (years 61–80).

Complex. Figure 4 shows that the patterns of vertically integrated OHU in both cases have many features in common. This suggests that the large-scale structure of the OHU in such experiments may not be very sensitive to the details of ΔT^* field. Furthermore, the patterns of OHU in our ocean-only experiments are dominated by heat uptake in the Southern Ocean, much like they are in AOGCMs in response to CO_2 increase (e.g., Exarchou et al. 2015; Kuhlbrodt et al. 2015; Morrison et al. 2016).

The AMOC strength, defined as the mean of the AMOC maximum values between 20° and 30°N in the Atlantic, decreases in both sets of sensitivity experiments (Fig. 5). The largest AMOC decrease, by 1.5–2 Sv ($1 \, \text{Sv} \equiv 10^6 \, \text{m}^3 \, \text{s}^{-1}$), is during the first two decades, followed by some recovery. [If both T^* and S^* were changed, then the AMOC decrease would likely be stronger, as shown by Xie and Vallis (2012).] It is interesting to note that there is no clear dependence of the AMOC decrease in these SST-forced sensitivity runs on

K_{GM} (Fig. 5) and, hence, on the AMOC strength in the control runs (discussed next). An AMOC/AMOC decline dependence, wherein models with stronger AMOC in the control runs show its larger decrease in climate change simulations, was found in some coupled models (e.g., Gregory et al. 2005; Winton et al. 2014; J. M. Gregory et al. 2017, unpublished manuscript). This suggests that the AMOC/AMOC decline dependence in such models arises from the feedback of SST to heat flux in the North Atlantic.

In what follows, we shall often compare and correlate relative variations of different quantities and parameters (AMOC strength, K_{GM}, OHU, etc.). The relative variation of a quantity or parameter χ is defined as its deviation from the mean, $\delta\chi = \chi - \langle\chi\rangle$, scaled by the mean $\langle\chi\rangle$ (i.e., relative variations of $\chi = \delta\chi/\langle\chi\rangle$). The averaging sign $\langle \dots \rangle$ will be dropped for simplicity. When discussing the results of numerical experiments, the averaging represents either the mean value of χ in the five control runs (such as in the case of, e.g., AMOC
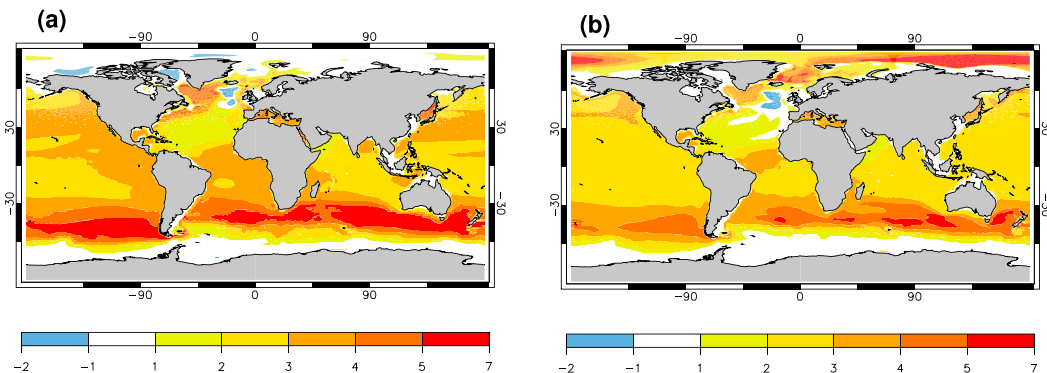

FIG. 4. Vertically integrated ocean heat uptake (GJ m^{-2}) in (a) Simple and (b) Complex sensitivity experiments with the scaling-factor γ in K_{GM} of 1.25 (relative to the corresponding control runs), averaged over the last 10 years (years 41–50).
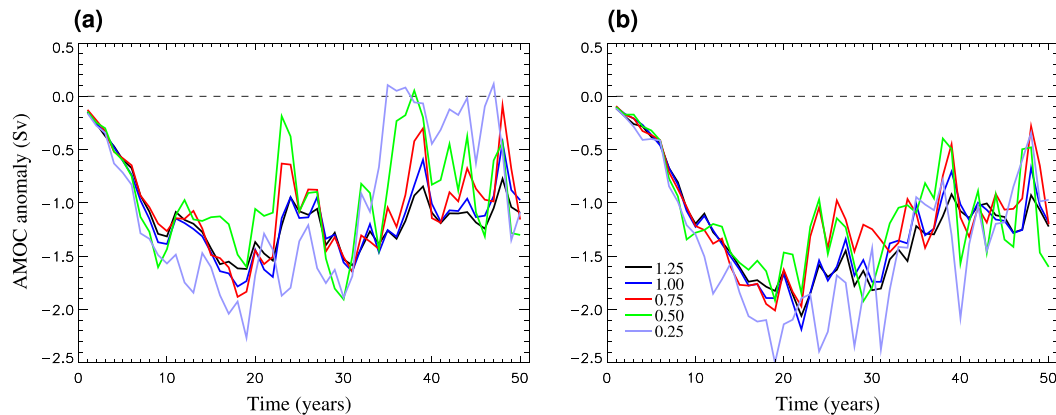
FIG. 5. Time series of the AMOC anomalies (Sv) in the (a) Simple and (b) Complex sets of sensitivity experiments for the different values of the scale-factor γ in the calculation of K_{GM}, ranging from 0.25 to 1.25. The corresponding values of zonal-mean K_{GM} for the Southern Ocean are shown in Fig. 2 (right). The mean control value of the AMOC is 14.2 Sv, which is within the ranges of the AMOC interannual variability estimated by the Rapid Climate Change (RAPID) array.

strength) or the mean χ difference between the five perturbation experiments and the corresponding control runs (such as in the case of, e.g., OHU).

3. Linking mesoscale eddy transfer to AMOC and OHU

a. Control simulations

Figure 6a presents the relative variations in some major components of the global ocean MOC (illustrated

schematically in Fig. 6b) in the control runs, plotted against the variations in K_{GM} averaged between 60° and 45°S, that is, roughly in the region of the Antarctic Circumpolar Current (ACC), as suggested by the scaling theory of Gnanadesikan (1999). As expected, the eddy-induced overturning in the Southern Ocean Ψ_{eddy} intensifies with the increase of K_{GM}. The lower southern overturning cell associated with the formation of the Antarctic Bottom Water (AABW) Ψ_{AABW} also becomes stronger with the increase of K_{GM}. However, the
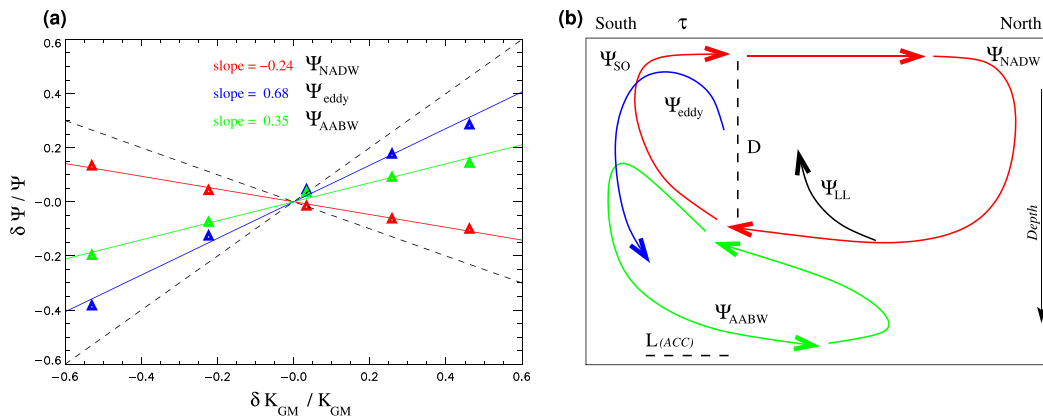

FIG. 6. (a) Relative variations in the strength of the major overturning cells in the five control experiments, plotted against the relative variations in the eddy transfer coefficient K_{GM} averaged between 60° and 45°S. The mean control values of these quantities, that is, relative to which the variations are computed, are $\Psi_{eddy} = -11.5$ Sv, $\Psi_{NADW} = 14.2$ Sv, $\Psi_{AABW} = -11.2$ Sv, and $K_{GM} = 388$ m^2 s^{-1}. The colored lines are regressions, whereas the dashed lines have slopes of 1 and -0.5. (Note that Ψ_{eddy} and Ψ_{AABW} are assumed counterclockwise, that is, negative, so that their negative changes, divided by the mean values, imply strengthening with K_{GM}). (b) Schematic diagram of the global ocean overturning cells (after Gnanadesikan 1999 and Marshall et al. 2017) associated with the eddy-induced overturning in the Southern Ocean Ψ_{eddy} (blue), the upper overturning in the North Atlantic Ψ_{NADW} (red), and the lower overturning cell originating from the south Ψ_{AABW} (green). The overturning Ψ_{NADW} is closed by the net dense-to-light water transformation in the upper Southern Ocean Ψ_{SO} and by deep water upwelling through the low-latitude thermocline Ψ_{LL}. The variable D is the mean depth of the upper overturning cell, whereas L and τ are, respectively, meridional scale and zonal wind stress within the latitudes of the ACC.

overturning rate in the upper Atlantic Ocean associated with the formation of the North Atlantic Deep Water (NADW) Ψ_{NADW}, or the AMOC strength, decreases with the increase in K_{GM}.

These results are, in general, consistent with Marshall et al. (2017). Building on their scaling relations, we next try to explain the regression slopes in Fig. 6a. Following Gnanadesikan (1999), we assume that Ψ_{NADW} is balanced by the net (mean plus eddy) overturning in the upper Southern Ocean (SO) Ψ_{SO} and also by the deep water upwelling at the low-latitude (LL) oceans Ψ_{LL} (Fig. 6b),

$$\Psi_{\text{NADW}} = \Psi_{\text{SO}} + \Psi_{\text{LL}}, \quad (9)$$

with

$$\Psi_{\text{NADW}} = c_1 D^2, \quad \Psi_{\text{SO}} = -\frac{\tau}{f} + \Psi_{\text{eddy}},$$

$$\Psi_{\text{LL}} = c_2 \frac{k_v}{D}, \quad \Psi_{\text{eddy}} = -K_{\text{GM}} \frac{D}{L}, \quad (10)$$

where, following Marshall et al. (2017), D is the mean depth of the upper overturning cell; L, f, and τ are the representative values of, respectively, the meridional scale, Coriolis parameter, and zonal wind stress (scaled by mean density) within the latitudes of the ACC; k_v is the vertical diffusivity; and c_1 and c_2 are dimensional constants. In (10), the scaling relation for Ψ_{LL} is based on the advective–diffusive balance (e.g., Gnanadesikan 1999). Following Marshall et al. (2017) and taking variations of both sides of (9) it is straightforward to show, using. (10), that

$$\frac{\delta D}{D}\left(1 + 2\frac{\Psi_{\text{NADW}}}{|\Psi_{\text{eddy}}|} + \frac{\Psi_{\text{LL}}}{|\Psi_{\text{eddy}}|}\right)$$
$$+ \frac{\delta K_{\text{GM}}}{K_{\text{GM}}} + \frac{\delta\tau}{f}\frac{1}{|\Psi_{\text{eddy}}|} - \frac{\delta k_v}{k_v}\frac{\Psi_{\text{LL}}}{|\Psi_{\text{eddy}}|} = 0. \quad (11)$$

Since $\delta\tau = 0$ (we do not vary wind in our experiments), (11) gives the following dependence of variations in the depth scale on the ocean mixing parameters:

$$\frac{\delta D}{D} = \left(1 + 2\frac{\Psi_{\text{NADW}}}{|\Psi_{\text{eddy}}|} + \frac{\Psi_{\text{LL}}}{|\Psi_{\text{eddy}}|}\right)^{-1}\left(\frac{\Psi_{\text{LL}}}{|\Psi_{\text{eddy}}|}\frac{\delta k_v}{k_v} - \frac{\delta K_{\text{GM}}}{K_{\text{GM}}}\right), \quad (12)$$

which suggests that D increases with the increase of vertical diffusivity but decreases with the increase of mesoscale eddy transfer. Since $\delta k_v \approx 0$ (same as Marshall et al. 2017; we do not vary the background vertical diffusivity), (12) becomes

$$\frac{\delta D}{D} = -\left(1 + 2\frac{\Psi_{\text{NADW}}}{|\Psi_{\text{eddy}}|} + \frac{\Psi_{\text{LL}}}{|\Psi_{\text{eddy}}|}\right)^{-1}\left(\frac{\delta K_{\text{GM}}}{K_{\text{GM}}}\right). \quad (13)$$

In climate change experiments based on AOGCMs, the depth of the AMOC has been shown to be correlated with the depth above which 80% of the total OHU is confined, or $D_{80\%}$ (Kostov et al. 2014). It is therefore reasonable to expect, based on (13), that $D_{80\%}$ in our SST-increase sensitivity experiments would correlate with K_{GM}. As we shall see, this is indeed the case.

Since $(\delta\Psi_{\text{NADW}}/\Psi_{\text{NADW}}) = 2\delta D/D$, (13) gives the following dependence of variations in deep water formation in the North Atlantic on K_{GM}:

$$\frac{\delta\Psi_{\text{NADW}}}{|\Psi_{\text{NADW}}|} = -\frac{2}{\left(1 + 2\frac{\Psi_{\text{NADW}}}{|\Psi_{\text{eddy}}|} + \frac{\Psi_{\text{LL}}}{|\Psi_{\text{eddy}}|}\right)}\frac{\delta K_{\text{GM}}}{K_{\text{GM}}}, \quad (14)$$

which is the same as (5) in Marshall et al. (2017), except for the term containing Ψ_{LL} in the denominator. Equation (14) suggests that with the increase of K_{GM}, Ψ_{NADW} should decrease at steady state. Given our model mean control values for Ψ_{NADW}, $|\Psi_{\text{eddy}}|$, and Ψ_{LL} of, respectively, 14.2, 11.5, and 3.2 Sv, this scaling predicts a slope of -0.53 between relative changes in Ψ_{NADW} and K_{GM}, whereas the model gives -0.24 (Fig. 6a). Other factors the same, scaling (14) predicts a smaller absolute slope for weaker Ψ_{eddy} and/or for stronger Ψ_{LL}. Physically, making Ψ_{LL} stronger would imply a more diffusive upper ocean (i.e., larger k_v), which would tend to decouple the deep water formation in the North Atlantic from the Southern Ocean (as illustrated in Fig. 6b).

A more favorable agreement with the numerical ocean model is obtained for the scaling that relates changes in the eddy-induced overturning in the Southern Ocean Ψ_{eddy} to changes in K_{GM}. Using the same assumptions and a similar procedure,[1] it is straightforward to show that

$$\frac{\delta\Psi_{\text{eddy}}}{|\Psi_{\text{eddy}}|} = -\frac{\left(2\frac{\Psi_{\text{NADW}}}{|\Psi_{\text{eddy}}|} + \frac{\Psi_{\text{LL}}}{|\Psi_{\text{eddy}}|}\right)}{\left(1 + 2\frac{\Psi_{\text{NADW}}}{|\Psi_{\text{eddy}}|} + \frac{\Psi_{\text{LL}}}{|\Psi_{\text{eddy}}|}\right)}\frac{\delta K_{\text{GM}}}{K_{\text{GM}}}, \quad (15)$$

which suggests that Ψ_{eddy} should intensify (become more negative; Fig. 6b) with the increase of K_{GM}, and that the magnitude of the corresponding slope should be less

---

[1] Noting that $\delta\Psi_{\text{eddy}}/|\Psi_{\text{eddy}}| = -\delta K_{\text{GM}}/K_{\text{GM}} - \delta D/D$ and using (13), one arrives at (15).
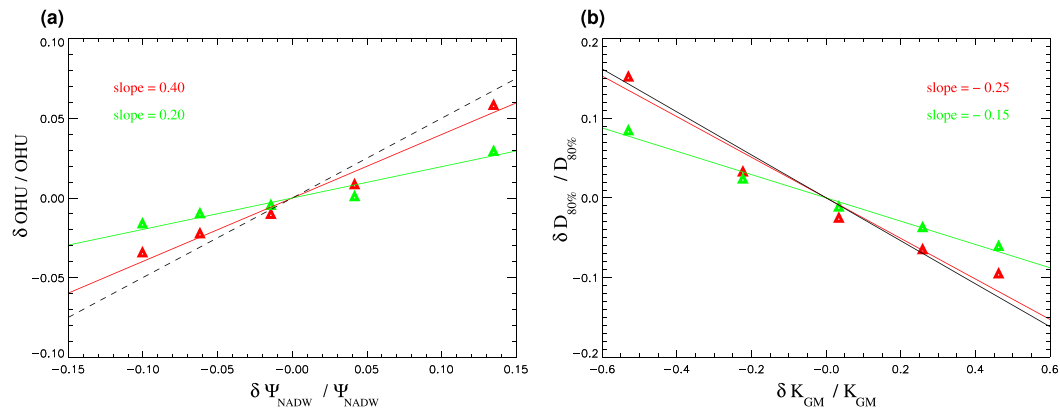
FIG. 7. Relative variations in the (a) OHU and (b) depth above which 80% of the total OHU is confined $D_{80\%}$ in the two sets of SST-perturbation experiments (Simple in red and Complex in green), plotted against relative variations in the corresponding control AMOC strength Ψ_{NADW} in (a) and control mesoscale eddy transfer K_{GM} in (b) in the Southern Ocean (between 60° and 45°S). In (a), the dashed line has the slope of 0.5. In (b), the black line has the slope of -0.27, corresponding to the relationship (12) between D and K_{GM} with the mean control values of Ψ_{NADW}, $|\Psi_{eddy}|$, and Ψ_{LL} of, respectively, 14.2, 11.5, and 3.2 Sv.

than 1. Physically, more negative Ψ_{eddy} would tend to reduce the rate of dense-to-light water transformation in the upper Southern Ocean (Fig. 6b). At steady state, this would have to be balanced by less light-to-dense water transformation in the north, that is, by weakening of Ψ_{NADW}. Given the mean control values of Ψ_{NADW}, $|\Psi_{eddy}|$, and Ψ_{LL}, this scaling predicts a slope of 0.73 between $\delta\Psi_{eddy}/\Psi_{eddy}$ and $\delta K_{GM}/K_{GM}$, while the model gives 0.68 (Fig. 6a).

The strength of the lower southern cell Ψ_{AABW} is expected to increase (i.e., become more negative) with the increase of mesoscale eddy activity in the Southern Ocean (Ito and Marshall 2008; Stanley and Saenko 2014). For the slope between $\delta\Psi_{AABW}/\Psi_{AABW}$ and $\delta K_{GM}/K_{GM}$, the theoretical arguments of Marshall et al. (2017)[2] predict 0.5, while the model gives 0.35 (Fig. 6a).

b. Response to SST perturbations

Introducing the perturbations discussed in section 2 to the control SSTs leads to OHU, which positively correlates with the control AMOC strength (Fig. 7a) and, hence, anticorrelates with the mesoscale eddy transfer (Fig. 6a). The warming penetrates deeper (i.e., $D_{80\%}$ is larger) under the smaller K_{GM} (Fig. 7b) and, hence, under the stronger AMOC. The changes in OHU and its penetration with depth also depend on the location of

the surface heat addition, that is, on the spatial structure of the imposed SST anomalies (Fig. 7; Simple vs Complex). In climate change simulations based on AOGCMs, such a sensitivity to the structure of surface warming may be a factor contributing to the scatter between OHUE (or $D_{80\%}$) and K_{GM}. Ocean model simulations presented by Huber and Zanna (2017) demonstrate that the impact of uncertainties in the surface fluxes projected by AOGCMs on OHU and its basin-scale patterns can be at least as large as the impact associated with uncertainties in ocean physics.

Thus, in our eddy-parameterizing ocean model, the values of K_{GM} set what can be called the effective heat capacity of the ocean (Kostov et al. 2014). Kostov et al. (2014) show a correlation between $D_{80\%}$ and the depth and the strength of the AMOC in AOGCMs. Figures 7 and 6a, combined with the scaling relations (13) and (14) (based on Marshall et al. 2017), suggest that these correlations could arise from the impact of the mesoscale eddy transfer on all these quantities. The deeper heat penetration under the smaller K_{GM} is found mostly at midlatitudes, particularly in the Southern Hemisphere (Fig. 8). In the North Atlantic, injection of heat to the deep ocean also strengthens with the decrease of K_{GM} (increase of AMOC strength; Fig. 8, bottom). However, the heat anomaly in the deep North Atlantic does not contribute much to the global zonal-mean temperature change (Fig. 8, top). We note that, despite representing a very idealized SST perturbation scenario (Simple), the changes in ocean temperature presented in Fig. 8 have many features in common with the corresponding changes simulated by AOGCMs [e.g., see Fig. 3 in Winton et al. (2014) and Fig. 4c in Kostov et al. (2014)].

---

[2] Marshall et al. (2017) build their arguments for changes in Ψ_{AABW} based on the scaling relation of Ito and Marshall (2008): $\Psi_{AABW} \sim -(k_v K_{GM})^{1/2}$. For relative changes it gives $\delta\Psi_{AABW}/|\Psi_{AABW}| = -(1/2)(\delta k_v/k_v + \delta K_{GM}/K_{GM})$. If relative changes in k_v, which may depend, for example, on changes in stratification, can be neglected, then one arrives at the scaling of Marshall et al. [2017, their (6)].
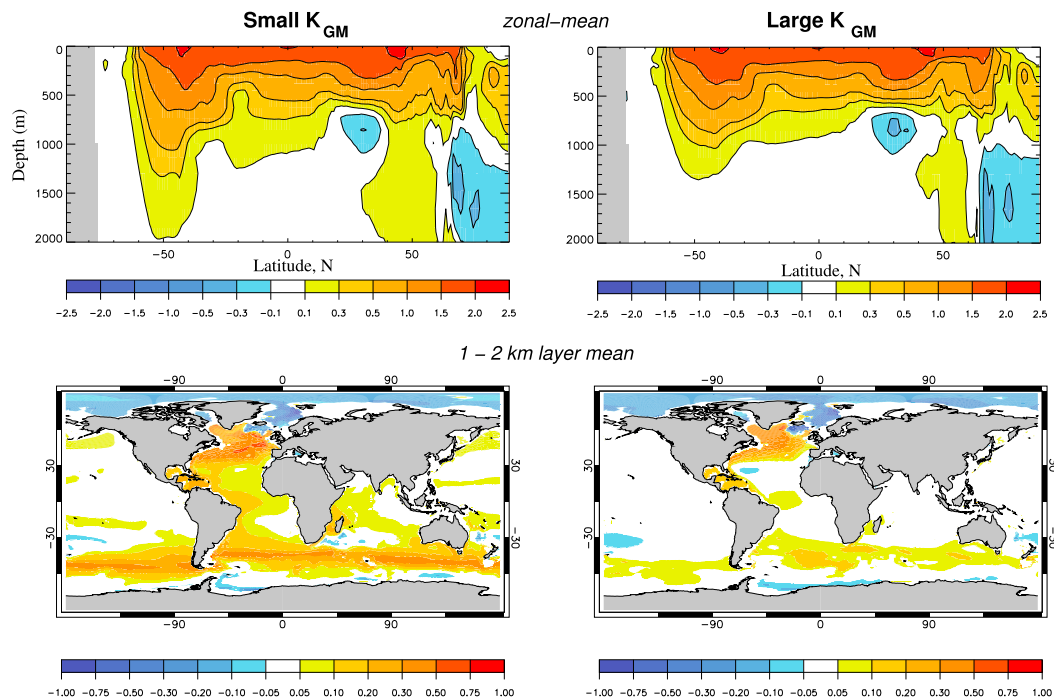
FIG. 8. Change in ocean temperature (K), averaged (top) zonally and (bottom) within the 1000–2000-m-depth layer and corresponding to the models with (left) the smallest K_{GM} and the strongest AMOC ($\gamma = 0.25$) and (right) the largest K_{GM} and the weakest AMOC ($\gamma = 1.25$). The temperature anomalies correspond to the Simple sensitivity experiments, relative to the corresponding control runs, for the final decade (years 41–50).

We next consider the main mechanisms causing the differences in vertical penetration of heat in the Simple experiments with the smallest and largest K_{GM} (similar conclusions apply to the Complex experiments). The mesoscale eddy transfer coefficient explicitly affects eddy-induced transport and, hence, it can affect the net heat advection (see also section 4). However, it can also affect the slope of isopycnals and stratification, thereby indirectly affecting the parameterized mixing processes and the associated OHU. As already noted, under the smaller K_{GM}, the heat anomalies penetrate deeper (Fig. 9, top) and are larger (Table 1). The parameterized mixing, which combines here all heat transport processes in the model other than the net advection (e.g., along-isopycnal diffusion, diapycnal mixing, convection, boundary layer mixing) dominates the subsurface ocean warming under both the small and the large K_{GM} (Fig. 9, bottom; Table 1). However, it is the changes in the eddy-induced heat divergence that account for most of the enhanced subsurface warming with the decrease of K_{GM}. In particular, while the resolved advection redistributes heat from the upper ocean into the interior, eddy advection generally tends to make the ocean interior colder (see Fig. 12b). In response to the SST perturbation, the subsurface ocean cooling by the eddy-induced advection increases more in the case of larger K_{GM} than

it does in the case of smaller K_{GM} (Fig. 9, middle; Table 1). The indirect influences of the mesoscale eddy transfer on the parameterized mixing also contribute to the enhanced interior ocean warming under the smaller K_{GM}.

Much of the above discussion of the global OHU mechanisms under the two extreme K_{GM} cases applies to the Southern Ocean, except that the heat convergence in this region may include contributions from lateral transports (as in any other open ocean region). In particular, in both K_{GM} cases, the subsurface heating in the Southern Ocean is also due to the mixing effects (Table 1). This includes contributions from somewhat decreased convection and along-isopycnal heat diffusion, which both flux heat upward. In particular, between 60° and 30°S, that is, where much of the OHU takes place (Fig. 4), the mixed layer depth (MLD) in September decreases by 8%–10%. The upward component of the along-isopycnal heat diffusion also decreases, mostly because of a decrease in the temperature gradient on isopycnals, as expected in a warmer ocean (Gregory 2000). The mean temperature gradient on the isopycnals that outcrop south of 35°S decreases by 13% under the largest K_{GM} and by 18% under the smallest K_{GM}. The slope of the isopycnals in the region decreases by 7%–8%, further contributing to the decrease
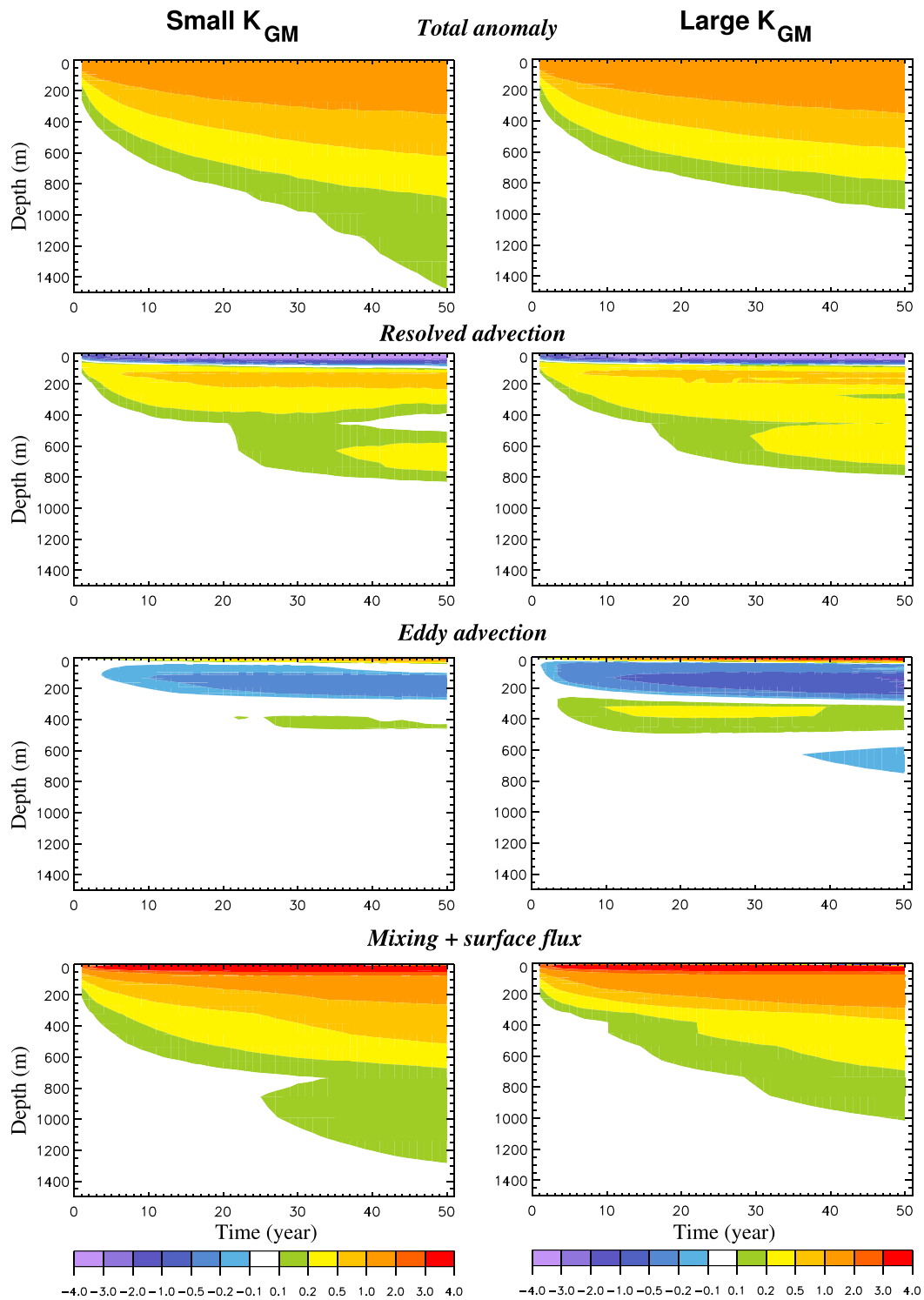
FIG. 9. Time evolution of the global ocean temperature profile changes (K) in the Simple experiments with (left) the smallest K_{GM} and (right) the largest K_{GM}, relative to the corresponding control runs: (top row) the total temperature change and the contributions to it due to (second row) the resolved advection, (third row) eddy advection, and (bottom row) all processes other than the net advection (including the surface heat flux anomaly in the uppermost layer).

TABLE 1. Change in ocean temperature within the 100–2000-m layer of the ocean after 50 years [K $(50 \text{ yr})^{-1}$] since the SST perturbation in Simple relative to Control (total), and contributions to it due to the model resolved advection (resolved adv), eddy advection (eddy adv), and all the parameterized mixing effects (mixing) for the global ocean (global), the Southern Ocean (south of 30°S), and northern North Atlantic (40°–70°N, 75°W–5°E). The upper numbers correspond to the case with the smallest K_{GM}, and lower numbers correspond to the case with the largest K_{GM}. For the Southern Ocean and North Atlantic, the presented changes in heat convergences combine contributions from the vertical and horizontal heat transport processes.

	Resolved adv	Eddy adv	Mixing	Total
Global	0.109	−0.023	0.305	0.391
	0.117	−0.077	0.294	0.334
Southern Ocean	−0.067	−0.077	0.642	0.498
	0.105	−0.267	0.579	0.417
North Atlantic	−1.119	−0.109	1.743	0.515
	−1.326	−0.156	1.771	0.289

of the upward component of the along-isopycnal heat diffusion. The changes in the net advection, while relatively small, tend to make the subsurface Southern Ocean colder, more so under the larger K_{GM}. This is mostly associated with the stronger cooling effect from the eddy advection (Table 1). Combined, this leads to enhanced warming in the subsurface Southern Ocean with the decrease of K_{GM}.

In the northern North Atlantic, the subsurface temperature changes are residuals of large in magnitude and opposite in sign changes in the net advection and mixing (Table 1). The decrease of advective heat convergence tends to make the subsurface North Atlantic colder (more so in the larger K_{GM} case), whereas the reduced deep convection tends to make it warmer. In both extreme K_{GM} cases, the winter MLD decreases by about 10% in the Atlantic north of 40°N. Locally, in the North Atlantic regions of deepest convection, the winter MLD decreases by several hundred meters (not shown).

c. Using passive tracers to test the OHUE–eddy transfer link

The anticorrelation between OHU and K_{GM} in our ocean model experiments is consistent with the anticorrelation between OHUE and K_{GM} in AOGCMs presented by Kuhlbrodt and Gregory (2012, their Fig. 3c), while the OHU–AMOC correlation is consistent with the OHUE–AMOC correlation in AOGCMs found by Kostov et al. (2014), Winton et al. (2014), and J. M. Gregory et al. (2017, unpublished manuscript). This is because SST in our ocean model is strongly constrained by restoring to prescribed T^*, so that the surface warming is essentially the same in the corresponding sets of SST-change experiments (and, hence,

OHU is the same as OHUE). If, instead, OHU were prescribed, one might expect less surface warming in the cases where the heat uptake penetrates deeper, corresponding here to the cases with smaller K_{GM} (Figs. 7b, 8) and stronger AMOC (Fig. 6a). This, combined with Kuhlbrodt and Gregory (2012), would further support the conclusion that at least some of the correlation between OHUE and AMOC in climate change simulations based on AOGCMs (e.g., Kostov et al. 2014; Winton et al. 2014; J. M. Gregory et al. 2017, unpublished manuscript) could be explained by the influence of the mesoscale eddy transfer coefficient on both OHUE and AMOC.

To test this hypothesis, we introduce a passive tracer. The tracer evolution is meant to represent the process of OHU. This is justified since much of the OHU process in AOGCMs can be simulated with a passive tracer forced at the surface (Gregory et al. 2016). Following Banks and Gregory (2006), we call it the passive anomaly temperature (PAT). PAT is initialized with a zero field and is transported within the model like potential temperature in the corresponding control run. Banks and Gregory (2006) found the vertical distribution of ocean temperature anomaly in their climate change simulation to be very similar to that of PAT. Given the same global-mean PAT, such as in the experiments described below, higher PAT in the upper ocean is meant to represent enhanced surface warming.

To obtain a preliminary insight, PAT is first forced with a constant and uniform surface flux of 2 W m^{-2}. This flux value roughly corresponds to the global-mean heat flux anomaly in the flux-anomaly-forced (faf) passive-heat experiment of the Flux-Anomaly-Forced Model Intercomparison Project (FAFMIP) described in Gregory et al. (2016). Figure 10 (top left) shows zonally averaged PAT at the end of the 50-yr-long control run with the smallest K_{GM}, and Fig. 10 (top right) shows the tracer difference between the two extreme control cases with the smallest and the largest K_{GM}. In support of our hypothesis, the control case with the smaller K_{GM} (stronger AMOC) has smaller values of PAT in the uppermost ocean (i.e., less near-surface "warming") and larger PAT in the deeper ocean (i.e., more "warming" in the oceanic interior; Fig. 10, top right). The deep ocean "warming" (i.e., larger PAT) under the smaller K_{GM} is particularly pronounced in the Southern Ocean and in the subpolar North Atlantic (Fig. 10, bottom).

To test our hypothesis under less idealized forcing, PAT is next forced with a nonuniform surface flux presented in Fig. 11a. This is the mean heat flux anomaly corresponding to the 1% yr^{-1} CO_2-increase experiment, averaged around the time of CO_2 doubling (years 61–80) and between 13 CMIP5 models. Its global-mean value is
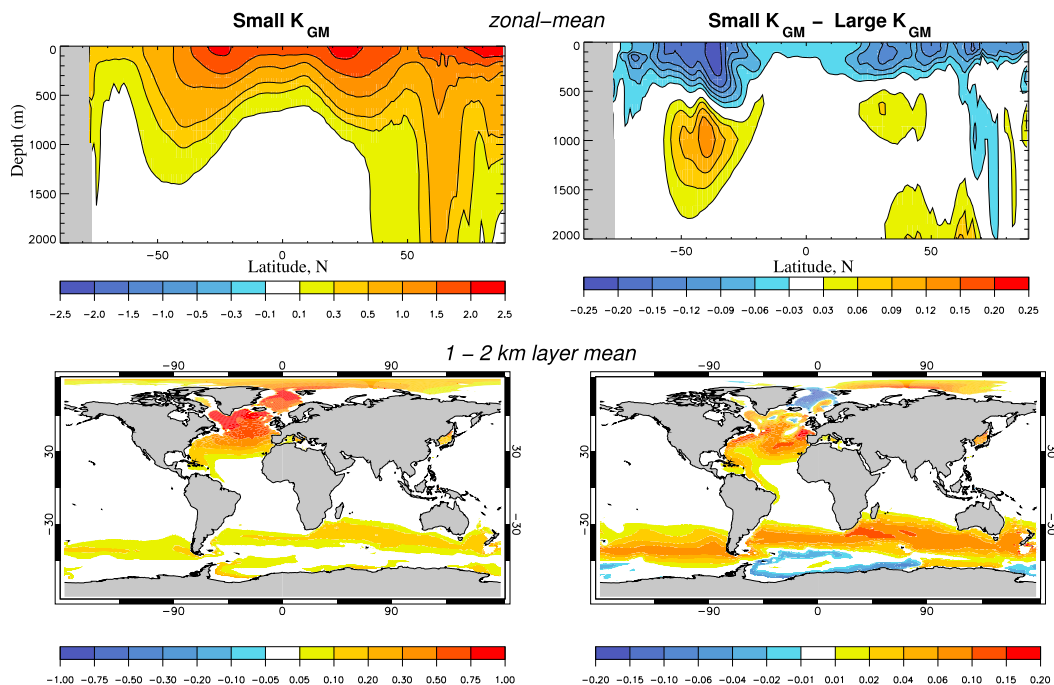
FIG. 10. PAT tracer forced with a uniform flux of $2\,\mathrm{W\,m^{-2}}$ (K), averaged (top) zonally and (bottom) within the 1000–2000-m-depth layer, corresponding to the control cases with (left) the smallest K_{GM} and (right) the difference between the cases with the smallest and the largest K_{GM}. The PATs represent decadal-mean values of the corresponding runs (years 41–50). Note the difference between the color scales in the left and right panels.

$1.86\,\mathrm{W\,m^{-2}}$. It has been adopted as the surface perturbation in some of the FAFMIP experiments [see Gregory et al. (2016) for more details]. The PAT forced with this flux is introduced in all five control experiments and run for 70 years (for consistency with the FAFMIP experimental design). The mean PAT in the upper 100 m of the ocean, which represents here the quantity *inversely proportional* to the OHUE, negatively correlates with the AMOC strength (Fig. 11b). This further supports our hypothesis that at least some of the correlation between OHUE and AMOC in climate simulations based on AOGCMs could be explained by the influence of the mesoscale eddy transfer coefficient on both OHUE and AMOC.

The upper-ocean PAT also scales with the global E_{eddy} (Fig. 11c) computed using (7), which in turn negatively correlates with the AMOC strength at steady state (Fig. 11d). The positive correlation between the upper-ocean PAT and E_{eddy} suggests that climate models with stronger eddy energy generation may tend to have smaller OHUE. It is interesting to note that among the two high-resolution climate models recently developed at the Geophysical Fluid Dynamics Laboratory (GFDL) and analyzed by Winton et al. (2014), the one with an ocean resolution of 0.1° has a smaller OHUE compared to that with a resolution of 0.25°. In addition, given that

E_{eddy} is closely related to the upward eddy buoyancy (heat) flux (e.g., Cessi 2008; see also section 4), it is interesting to note that the GFDL's 0.1° model has a stronger upward eddy heat flux in the upper ocean, compared to the 0.25° model (Griffies et al. 2015).

4. Linking vertical advective heat flux to OHU and AMOC

The eddy-induced vertical velocity w_{eddy} is directly related to the mesoscale eddy transfer (Gent et al. 1995) $w_{\mathrm{eddy}} = \nabla K_{\mathrm{GM}}\mathbf{S}$, where $\mathbf{S} = -\nabla\overline{b}/\overline{b}_z$ is the slope of mean isopycnals. It is therefore reasonable to expect that the net vertical advective heat transport $\mathcal{H}$, which is given by the sum of heat transports due to the resolved $\overline{\mathcal{H}}$ and eddy-induced $\mathcal{H}_{\mathrm{eddy}}$ circulations, that is,

$$\mathcal{H}(z) = \overline{\mathcal{H}} + \mathcal{H}_{\mathrm{eddy}} = C\iint(\overline{w} + w_{\mathrm{eddy}})\overline{\theta}\,dA, \quad (16)$$

is also linked to the OHU. In (16), C is the volumetric heat capacity of seawater; $\overline{w}$ is the resolved vertical velocity, which can be affected by K_{GM} implicitly; and $\overline{\theta}$ is the potential temperature. Figure 12a shows that, indeed, the net OHU scales with the net downward advective heat transport across the 100-m depth ($-\mathcal{H}$) in
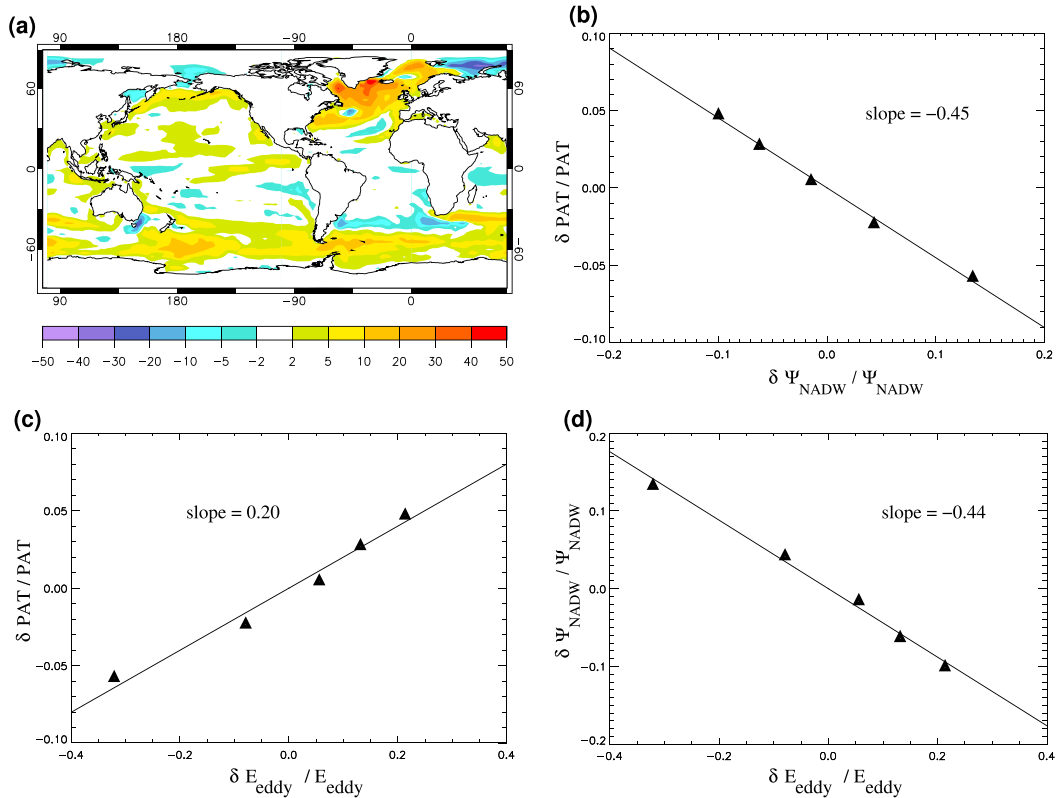
FIG. 11. (a) Nonuniform surface heat flux (W m^{-2}) used to force PAT in the second set of passive tracer experiments. It corresponds to CO_2 doubling in the 1% yr^{-1} CO_2-increase experiment, averaged between 13 CMIP5 models and adopted as one of the surface perturbations in FAFMIP [see Gregory et al. (2016) for more details]. (b)–(d) The corresponding relative variations of the global-mean PAT in the upper 0–100-m layer plotted against relative variations of the AMOC strength Ψ_{NADW} in (b) and the global rate with which the Gent and McWilliams (1990) scheme extracts potential energy from E_{eddy} in (c) in the control runs. Shown in (d) are the relative variations of Ψ_{NADW} plotted against the relative variations of E_{eddy} in the control runs.

our control experiments. This correlation holds for other depths, too; the depth of 100 m is selected because this is where $|\mathcal{H}|$ is the largest (Fig. 12b, black curves). The shape of $\mathcal{H}(z)$ suggests that it redistributes heat from the upper ocean into the deeper oceanic interior, thereby making the former colder and the latter warmer. In our control model runs, the increase in the net downward advective heat transport with the decrease of K_{GM} is mostly, but not only, due to the decrease of $\mathcal{H}_{eddy}$ (Fig. 12b, blue curves). The upward direction of the eddy-induced heat transport is consistent with the notion that mesoscale eddies flux buoyancy upward on global mean, thereby removing potential energy. In models where ocean mesoscale eddy effects are resolved to some extent, the eddy heat transport is also found to be directed upward (Wolfe et al. 2008; Morrison et al. 2013; Kuhlbrodt et al. 2015; Griffies et al. 2015).

The direction of the vertical heat transport associated with $\overline{w}$ is expected to be downward on global mean, as first found by Gregory (2000). One reason for this is that

the vertical buoyancy transport due to the large-scale ocean circulation is linked to the mean wind power input to the ocean (Gnanadesikan et al. 2005; Gregory and Tailleux 2011). Therefore, to generate potential energy, the mean buoyancy transport is expected to be directed downward. In our model, the direction, structure, and magnitude of $\overline{\mathcal{H}}$ are broadly in agreement with Cummins et al. (2016; Fig. 12b). Cummins et al. (2016) made their estimates of the part of $\mathcal{H}$ associated with the large-scale ocean circulation using the linear vorticity balance ($f\overline{w}_z = \beta\overline{v}$) and observational estimates of Ekman pumping, meridional geostrophic velocity (used for $\overline{v}$ below the mixed layer), and ocean temperature. They found the deepest penetration of the Ekman component of $\overline{w}$ and the associated heat flux in the Southern Ocean, particularly at the Drake Passage latitudes where the zonal integral of zonal pressure gradient (i.e., zonal integral of meridional geostrophic velocity) vanishes above roughly the 2000-m depth. This is consistent with our findings (not shown). However,
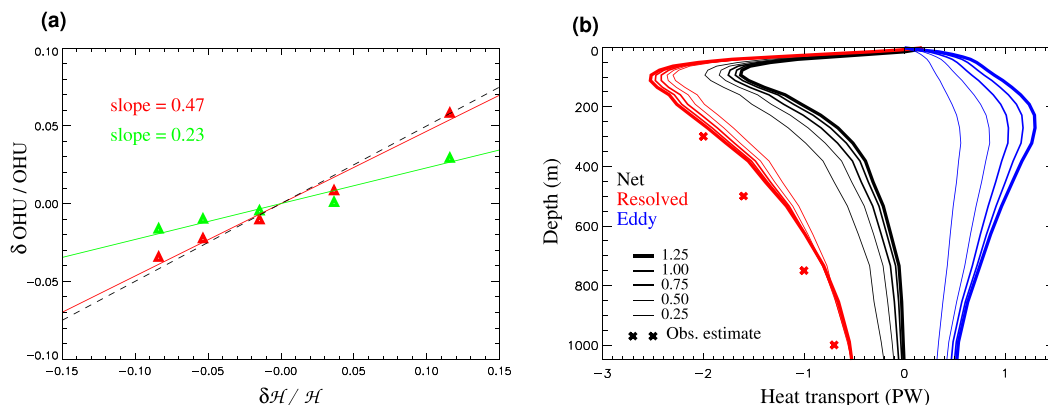
FIG. 12. (a) Relative variations in the OHU in the two sets of SST-perturbation experiments (Simple in red and Complex in green), plotted against relative variations in the net downward advective (resolved plus eddy) heat transport across about 100-m depth in the five control runs $-\mathcal{H}(100)$. (b) Vertical advective heat transport $\mathcal{H}(z)$ in the upper 1 km of the ocean (positive upward) for the five control model runs representing the resolved advection $\overline{\mathcal{H}}$ (red), the eddy-induced advection $\mathcal{H}_{\text{eddy}}$ (blue), and the net advection ($\mathcal{H} = \overline{\mathcal{H}} + \mathcal{H}_{\text{eddy}}$; black). Different curves correspond to different values of the scale-factor γ in the calculation of K_{GM}, which decreases from 1.25 (thickest curves) to 0.25 (thinnest curves). The corresponding values of zonal-mean K_{GM} for the Southern Ocean are shown in Fig. 2 (right). Also plotted, for comparison with the resolved advective heat transport, are the values of the time-mean advective heat transport estimate at several depths from Cummins et al. (2016); these are obtained using observations and geostrophic vorticity balance.

the upward heat transport due to the eddy-induced circulation tends to cancel a substantial fraction of the downward heat transport associated with the mean circulation (Fig. 12b). As a result, the net downward advective heat transport is relatively weak below the upper several hundred meters (Fig. 12b), consistent with Griffies et al. (2015, their Fig. 13). With the increase of K_{GM}, $|\overline{\mathcal{H}}|$ somewhat increases in the upper ocean (by about 10% between the two extreme control cases). This may be related to the tendency for the mean advective heat transport to compensate for the increase in the eddy heat advection, which would be expected if the net advection (mean plus eddy) were the only mechanism transporting heat vertically (i.e., if all mixing processes were weak on the global mean). Decomposing the change in $\overline{\mathcal{H}}$ into the contributions arising because of changes in the resolved circulation, temperature, and their co-changes (i.e., $\Delta \overline{\mathcal{H}} = C \iint (\overline{w} \Delta \overline{\theta} + \Delta \overline{w} \overline{\theta} + \Delta \overline{w} \Delta \overline{\theta}) \, dA$), it is found that these three terms almost equally contribute to $\Delta \overline{\mathcal{H}}$ around the 150-m depth. Below this depth the co-change term acts to decrease $\Delta \overline{\mathcal{H}}$, whereas the other two terms act to increase it (not shown).

From Figs. 7a and 12a, it is clear that Ψ_{NADW} and the net downward advective heat transport in the upper ocean correlate, with the slope of regression line between their relative changes being close to 1 (not shown). This suggests that the AMOC, if viewed as the global ocean overturning cell in the upper ocean (Fig. 7b), fluxes heat downward. This is less obvious than the injection of heat *anomalies* to the deep

Atlantic by the AMOC in climate change experiments [e.g., see Fig. 4c in Kostov et al. (2014) or bottom panels of our Figs. 8 and 10]. For the AMOC to flux heat downward at steady state in a control experiment, the temperature of its sinking branch must be warmer than the temperature of its upwelling branch.

To understand better the apparent connection between the AMOC strength and the global vertical advective heat transport given by (16), it is useful to consider a streamfunction in depth–temperature coordinates $\Psi^{z\theta}$ (e.g., Nycander et al. 2007; Zika et al. 2013, 2015). It can be computed as follows:

$$\Psi^{z\theta} = \iint_{A(\theta' \leq \theta)} w \, dA. \tag{17}$$

In (17), the net vertical velocity w ($= \overline{w} + w_{\text{eddy}}$) is integrated at constant depths over the ocean areas A where the potential temperature θ' is less than or equal to the targeted temperature θ. Figure 13 presents the depth–temperature streamfunction for the control runs with the smallest and largest K_{GM}. The net $\Psi^{z\theta}$ (Fig. 13, top) is the sum of the corresponding resolved $\overline{\Psi}^{z\theta}$ (Fig. 13, middle) and eddy-induced $\Psi_{\text{eddy}}^{z\theta}$ (Fig. 13, bottom) streamfunctions. In the adopted convention, the mostly positive $\overline{\Psi}^{z\theta}$ implies a downward heat transport associated with $\overline{w}$, whereas the negative $\Psi_{\text{eddy}}^{z\theta}$ implies an upward heat transport associated with w_{eddy}. Both $\overline{\Psi}^{z\theta}$ and $\Psi_{\text{eddy}}^{z\theta}$ are quite
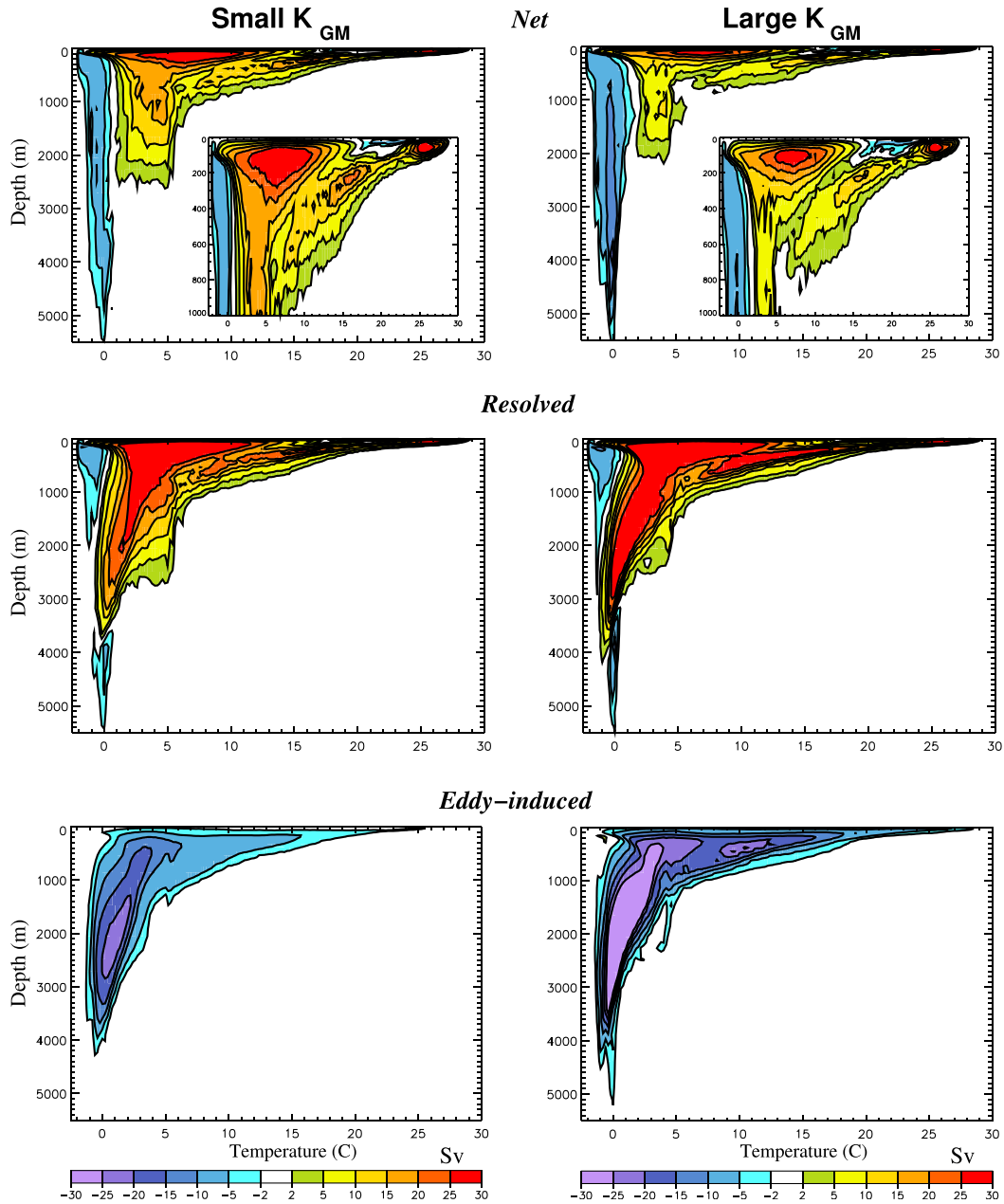
FIG. 13. Global ocean overturning circulation (Sv) in depth–temperature coordinates (positive clockwise), corresponding to the (top) net (resolved plus eddy induced) velocity, (middle) the resolved velocity, and (bottom) eddy-induced velocity in the control runs with (left) the smallest K_{GM} ($\gamma = 0.25$) and (right) the largest K_{GM} ($\gamma = 1.25$). The inserts in the top panels show the corresponding plots for the upper 1000 m of the ocean.

strong and penetrate deeply. However, because of the considerable cancellation between them, the positive part of their sum (i.e., $\Psi^{z\theta}$) is relatively weak below the upper several hundred meters. The degree of the $\overline{\Psi}^{z\theta} + \Psi^{z\theta}_{\text{eddy}}$ cancellation increases with the increase of the mesoscale eddy transfer (Fig. 13, top), same as in the corresponding vertical heat transports (Fig. 12b).

We next investigate the contributions to $\Psi^{z\theta}$ arising from the vertical motions in the Northern and Southern Hemispheres. While such a partitioning of $\Psi^{z\theta}$ would lead to circulation cells that are not closed when considered separately for each hemisphere [see Fig. 12b in Hogg et al. (2017)], and, hence, it cannot be used to rigorously attribute heat transport to a particular branch of the circulation, it may still provide some
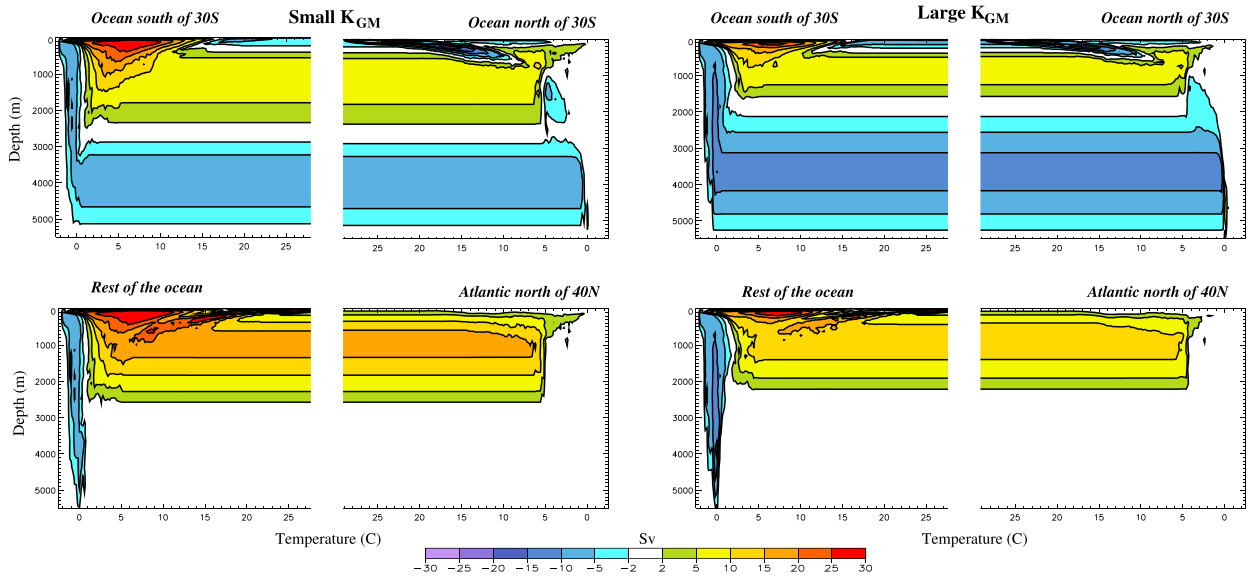
FIG. 14. The net (resolved plus eddy) ocean overturning circulations (Sv) in depth–temperature coordinates corresponding to the top panels in Fig. 12, but separated into contributions from (top) the ocean north of 30°S and south of 30°S and (bottom) the Atlantic north of 40°N and the rest of the ocean. The plots correspond to the control runs with (left) the smallest K_{GM} ($\gamma = 0.25$) and (right) the largest K_{GM} ($\gamma = 1.25$).

insight on the contribution of the AMOC to $\Psi^{z\theta}$. To see this, $\Psi^{z\theta}$ is separated here into contributions from the Southern Ocean and the rest of the ocean (Fig. 14, top), and also from the northern North Atlantic and the rest of the ocean (Fig. 14, bottom). These separations suggest that the net positive $\Psi^{z\theta}$ in the upper ocean (Fig. 13, top), which gives rise to the net downward advective heat transport (Fig. 12b), is partly closed in the Southern Ocean (Fig. 14, top), where the water subducting north of the ACC is warmer than the water upwelling south of it. In addition, it is closed through the joint effect of the water sinking in the North Atlantic being somewhat warmer than its compensating upwelling elsewhere (Fig. 14, bottom), mostly in the Southern Ocean. This further suggests that the AMOC in our control runs contributes to the net downward advective transport of heat. A decrease of the AMOC strength, induced in our experiments by making the mesoscale eddy transfer larger, results in a weaker net downward advective transport of heat.

As a final remark here, we note that the negative part of $\Psi^{z\theta}$ around 0°C is mostly associated with the circulation of the AABW. It also has contributions from both $\overline{\Psi}^{z\theta}$ and $\Psi^{z\theta}_{\text{eddy}}$ (Fig. 13), fluxing heat upward. However, because it is confined within small temperature ranges, its contribution to the vertical advective heat transport in the upper ocean in relatively small (although it does play a major role in the abyss, where the associated upward heat flux must be balanced by downward heat fluxes from some other processes, such as small-scale

mixing). As expected, the corresponding cell of $\Psi^{z\theta}$ is closed mostly outside of the northern North Atlantic (Fig. 14).

5. Discussion and conclusions

AOGCM-based studies show a correlation between the AMOC and OHUE (Kostov et al. 2014; Winton et al. 2014; J. M. Gregory et al. 2017, unpublished manuscript) and an anticorrelation between the mesoscale eddy transfer coefficient and OHUE (Kuhlbrodt and Gregory 2012). However, how the AMOC is related to OHUE and why there is a correlation between the AMOC strength and OHUE in climate simulations based on AOGCMs had not been comprehensively explained. Here, we argue that at least some of the AMOC–OHUE correlation in AOGCMs could be explained by the influence of the mesoscale eddy transfer in the Gent and McWilliams (1990) parameterization on both OHUE and AMOC. Our arguments are based, in part, on the finding (e.g., Gregory et al. 2016) that much of the OHU in AOGCMs can be modeled with a passive tracer forced at the surface. We show that given the same prescribed surface flux, the tracer values decrease near the surface and increase in the deep ocean with the decrease of K_{GM} (with the strengthening of AMOC). In climate change simulations based on AOGCMs, such a vertical distribution of OHU corresponds to models with larger OHUE and stronger AMOC (J. M. Gregory et al. 2017, unpublished

manuscript). While there are many parameterizations in ocean models with uncertain parameters, the systematic way in which the mesoscale eddy transfer affects both the AMOC and OHUE is supported by the numerical results and theoretical arguments. We find that while most of the OHU is due to mixing processes in the global mean, it is the changes in the eddy-induced advection that contribute more to the weaker ocean interior warming under the larger mesoscale eddy transfer.

In addition, we show that the OHU in our SST-perturbation experiments correlates with the net downward advective transport of heat in the control model runs (or with the net upward heat flux by all other processes combined). Thus, changes in the net downward heat advection, at least if induced by changes in the mesoscale eddy transfer, scale with changes in the AMOC strength. To show that the AMOC in our model does add to the net global downward advective transport of heat, we use overturning streamfunction in depth–temperature coordinates and separate it into contributions from several regions. That the AMOC transports heat downward can also be inferred from the finding of Gregory et al. (2016) that the change in heat redistribution in their faf-heat experiment, arising mainly from the weakening of the AMOC, causes cooling at all depths in the north (their Fig. 11i), leading to a net cooling below about 1500 m (their Fig. 11g).

The link between the net downward heat advection and the AMOC strength may hold in other models, too, and not necessarily only in those that explicitly parameterize mesoscale eddy effects. For example, in the suite of the GFDL climate models analyzed by Griffies et al. (2015) the net (mean plus eddy) downward advective heat flux decreases with the increase of resolution from 1° to 0.1° (their Fig. 12) and so does the AMOC strength. Some of our other results, such the decrease of OHUE with the increase of eddy energy generation by baroclinic instability, may also find applicability when interpreting climate change simulations with high-resolution ocean components.

REFERENCES

Banks, H. T., and J. M. Gregory, 2006: Mechanisms of ocean heat uptake in a coupled climate model and the implications for tracer based predictions of ocean heat uptake. *Geophys. Res. Lett.*, **33**, L07608, https://doi.org/10.1029/2005GL025352.

Bryan, K., J. K. Dukowicz, and R. D. Smith, 1999: On the mixing coefficient in the parameterization of bolus velocity. *J. Phys. Oceanogr.*, **29**, 2442–2456, https://doi.org/10.1175/1520-0485(1999)029<2442:OTMCIT>2.0.CO;2.

Cessi, P., 2008: An energy-constrained parameterization of eddy buoyancy flux. *J. Phys. Oceanogr.*, **38**, 1807–1819, https://doi.org/10.1175/2007JPO3812.1.

Chelton, D. B., M. G. Schlax, and R. M. Samelson, 2011: Global observations of nonlinear mesoscale eddies. *Prog. Oceanogr.*, **91**, 167–216, https://doi.org/10.1016/j.pocean.2011.01.002.

Cummins, P. F., D. Masson, and O. A. Saenko, 2016: Vertical heat flux in the ocean: Estimates from observations and from a coupled general circulation model. *J. Geophys. Res. Oceans*, **121**, 3790–3802, https://doi.org/10.1002/2016JC011647.

Exarchou, E., T. Kuhlbrodt, J. M. Gregory, and R. S. Smith, 2015: Ocean heat uptake processes: A model intercomparison. *J. Climate*, **28**, 887–908, https://doi.org/10.1175/JCLI-D-14-00235.1.

Gaspar, P., Y. Grégoris, and J.-M. Lefevre, 1990: A simple eddy kinetic energy model for simulations of the oceanic vertical mixing: Tests at station Papa and long-term upper ocean study site. *J. Geophys. Res.*, **95**, 16179–16193, https://doi.org/10.1029/JC095iC09p16179.

Gent, P. R., and J. C. McWilliams, 1990: Isopycnal mixing in ocean general circulation models. *J. Phys. Oceanogr.*, **20**, 150–155, https://doi.org/10.1175/1520-0485(1990)020<0150:IMIOCM>2.0.CO;2.

——, J. Willebrand, T. J. McDougall, and J. C. McWilliams, 1995: Parameterizing eddy-induced tracer transports in ocean circulation models. *J. Phys. Oceanogr.*, **25**, 463–474, https://doi.org/10.1175/1520-0485(1995)025<0463:PEITTI>2.0.CO;2; Corrigendum, **25**, 1365, https://doi.org/10.1175/1520-0485(1995)025<1365:>2.0.CO;2.

Gnanadesikan, A., 1999: A simple predictive model for the structure of the oceanic pycnocline. *Science*, **283**, 2077–2079, https://doi.org/10.1126/science.283.5410.2077.

——, R. D. Slater, P. S. Swathi, and G. K. Vallis, 2005: The energetics of ocean heat transport. *J. Climate*, **18**, 2604–2616, https://doi.org/10.1175/JCLI3436.1.

——, M.-A. Pradal, and R. Abernathey, 2015: Isopycnal mixing by mesoscale eddies significantly impacts oceanic anthropogenic carbon uptake. *Geophys. Res. Lett.*, **42**, 4249–4255, https://doi.org/10.1002/2015GL064100.

Gregory, J. M., 2000: Vertical heat transports in the ocean and their effect on time-dependent climate change. *Climate Dyn.*, **16**, 501–515, https://doi.org/10.1007/s003820000059.

——, and R. Tailleux, 2011: Kinetic energy analysis of the response of the Atlantic meridional overturning circulation to CO_2-forced climate change. *Climate Dyn.*, **37**, 893–914, https://doi.org/10.1007/s00382-010-0847-6.

——, and Coauthors, 2005: A model intercomparison of changes in the Atlantic thermohaline circulation in response to increasing atmospheric CO_2 concentration. *Geophys. Res. Lett.*, **32**, L12703, https://doi.org/10.1029/2005GL023209.

——, and Coauthors, 2016: The Flux-Anomaly-Forced Model Intercomparison Project (FAFMIP) contribution to CMIP6: Investigation of sea-level and ocean climate change in response

to CO_2 forcing. *Geosci. Model Dev.*, **9**, 3993–4017, https://doi.org/10.5194/gmd-9-3993-2016.

Griffies, S. M., and Coauthors, 2015: Impacts on ocean heat from transient mesoscale eddies in a hierarchy of climate models. *J. Climate*, **28**, 952–977, https://doi.org/10.1175/JCLI-D-14-00353.1.

Hogg, A. M., P. Spence, O. A. Saenko, and S. M. Downes, 2017: The energetics of Southern Ocean upwelling. *J. Phys. Oceanogr.*, **47**, 135–153, https://doi.org/10.1175/JPO-D-16-0176.1.

Huber, M. B., and L. Zanna, 2017: Drivers of uncertainty in simulated ocean circulation and heat uptake. *Geophys. Res. Lett.*, **44**, 1402–1413, https://doi.org/10.1002/2016GL071587.

Ito, T., and J. Marshall, 2008: Control of lower-limb overturning circulation in the Southern Ocean by diapycnal mixing and mesoscale eddy transfer. *J. Phys. Oceanogr.*, **38**, 2832–2845, https://doi.org/10.1175/2008JPO3878.1.

Kostov, Y., K. C. Armour, and J. Marshall, 2014: Impact of the Atlantic meridional overturning circulation on ocean heat storage and transient climate change. *Geophys. Res. Lett.*, **41**, 2108–2116, https://doi.org/10.1002/2013GL058998.

Kuhlbrodt, T., and J. M. Gregory, 2012: Ocean heat uptake and its consequences for the magnitude of sea level rise and climate change. *Geophys. Res. Lett.*, **39**, L18608, https://doi.org/10.1029/2012GL052952.

——, ——, and L. C. Shaffrey, 2015: A process-based analysis of ocean heat uptake in an AOGCM with an eddy-permitting ocean component. *Climate Dyn.*, **45**, 3205–3226, https://doi.org/10.1007/s00382-015-2534-0.

Levitus, S., and Coauthors, 2012: World ocean heats content and thermosteric sea level change (0–2000 m), 1955–2010. *Geophys. Res. Lett.*, **39**, L10603, https://doi.org/10.1029/2012GL051106.

Madec, G., and Coauthors, 2012: NEMO ocean engine, version 3.4. Institut Pierre-Simon Laplace Note du Pole de Modélisation 27, 367 pp.

Marshall, D. P., and L. Zanna, 2014: A conceptual model of ocean heat uptake under climate change. *J. Climate*, **27**, 8444–8465, https://doi.org/10.1175/JCLI-D-13-00344.1.

Marshall, J., J. R. Scott, K. C. Armour, J.-M. Campin, M. Kelley, and A. Romanou, 2015: The ocean's role in the transient response of climate to abrupt greenhouse gas forcing. *Climate Dyn.*, **44**, 2287–2299, https://doi.org/10.1007/s00382-014-2308-0.

——, ——, A. Romanou, M. Kelley, and A. Leboissetier, 2017: The dependence of the ocean's MOC on mesoscale eddy diffusivities: A model study. *Ocean Modell.*, **111**, 1–8, https://doi.org/10.1016/j.ocemod.2017.01.001.

Morrison, A. K., O. A. Saenko, A. M. Hogg, and P. Spence, 2013: The role of vertical eddy flux in Southern Ocean heat uptake. *Geophys. Res. Lett.*, **40**, 5445–5450, https://doi.org/10.1002/2013GL057706.

——, S. M. Griffies, M. Winton, W. G. Anderson, and J. L. Sarmiento, 2016: Mechanisms of Southern Ocean heat uptake and transport in a global eddying climate model. *J. Climate*, **29**, 2059–2075, https://doi.org/10.1175/JCLI-D-15-0579.1.

Nycander, J., J. Nilsson, K. Döös, and G. Broström, 2007: Thermodynamic analysis of ocean circulation. *J. Phys. Oceanogr.*, **37**, 2038–2052, https://doi.org/10.1175/JPO3113.1.

Redi, M. H., 1982: Oceanic isopycnal mixing by coordinate rotation. *J. Phys. Oceanogr.*, **12**, 1154–1158, https://doi.org/10.1175/1520-0485(1982)012<1154:OIMBCR>2.0.CO;2.

Simmons, H. L., S. R. Jayne, L. C. St. Laurent, and A. J. Weaver, 2004: Tidally driven mixing in a numerical model of the ocean general circulation. *Ocean Modell.*, **6**, 245–263, https://doi.org/10.1016/S1463-5003(03)00011-8.

Stanley, G. J., and O. A. Saenko, 2014: Bottom-enhanced diapycnal mixing driven by mesoscale eddies: Sensitivity to wind energy supply. *J. Phys. Oceanogr.*, **44**, 68–85, https://doi.org/10.1175/JPO-D-13-0116.1.

Visbeck, M., J. Marshall, T. Haine, and M. Spall, 1997: Specification of eddy transfer coefficients in coarse-resolution ocean circulation models. *J. Phys. Oceanogr.*, **27**, 381–402, https://doi.org/10.1175/1520-0485(1997)027<0381:SOETCI>2.0.CO;2.

Winton, M., W. G. Anderson, T. L. Delworth, S. M. Griffies, W. J. Hurlin, and A. Rosati, 2014: Has coarse ocean resolution biased simulations of transient climate sensitivity? *Geophys. Res. Lett.*, **41**, 8522–8529, https://doi.org/10.1002/2014GL061523.

Wolfe, C. L., P. Cessi, J. L. McClean, and M. E. Maltrud, 2008: Vertical heat transport in eddying ocean models. *Geophys. Res. Lett.*, **33**, L19708, https://doi.org/10.1029/2008GL036138.

Wunsch, C., and R. Ferrari, 2004: Vertical mixing, energy, and the general circulation of the oceans. *Annu. Rev. Fluid Mech.*, **36**, 281–314, https://doi.org/10.1146/annurev.fluid.36.050802.122121.

Xie, P., and G. K. Vallis, 2012: The passive and active nature of ocean heat uptake in idealized climate change experiments. *Climate Dyn.*, **38**, 667–684, https://doi.org/10.1007/s00382-011-1063-8.

Yang, D., and O. A. Saenko, 2012: Ocean heat transport and its projected change in CanESM2. *J. Climate*, **25**, 8148–8163, https://doi.org/10.1175/JCLI-D-11-00715.1.

Zika, J. D., W. P. Sijp, and M. H. England, 2013: Vertical heat transport by ocean circulation and the role of mechanical and haline forcing. *J. Phys. Oceanogr.*, **43**, 2095–2112, https://doi.org/10.1175/JPO-D-12-0179.1.

——, F. Laliberté, L. R. Mudryk, W. P. Sijp, and A. J. G. Nurser, 2015: Changes in ocean vertical heat transport with global warming. *Geophys. Res. Lett.*, **42**, 4940–4948, https://doi.org/10.1002/2015GL064156.